THE JOURNAL OF PHYSICAL CHEMISTRY A
A JOURNAL OF THE AMERICAN CHEMICAL SOCIETY

pubs.acs.org/JPCA Article

Expanded Inverse-Sandwich Complexes of Lanthanum Borides: $La_2B_{10}^-$ and $La_2B_{11}^-$

Published as part of The Journal of Physical Chemistry virtual special issue "Alexander Boldyrev Festschrift".

Zhi-Yu Jiang,[#] Teng-Teng Chen,[#] Wei-Jia Chen, Wan-Lu Li,* Jun Li,* and Lai-Sheng Wang*

Cite This: *J. Phys. Chem. A* 2021, 125, 2622–2630 Read Online

ACCESS | Metrics & More | Article Recommendations | Supporting Information

ABSTRACT: Inverse-sandwich structures have been observed recently for dilanthanide boride clusters, in which two Ln atoms sandwich a monocyclic B_x ring for $x = 7-9$. An interesting question is if larger B_x rings are possible to form such inverse-sandwich clusters. Here we address this question by investigating $La_2B_{10}^-$ and $La_2B_{11}^-$ using photoelectron spectroscopy and *ab initio* quantum chemical calculations. Photoelectron spectra of $La_2B_{10}^-$ and $La_2B_{11}^-$ show complicated, but well-resolved, spectral features that are used to compare with theoretical calculations. We have found that global minimum structures of the two clusters are based on the octa-boron ring. The global minimum of $La_2B_{10}^-$ consists of two chiral enantiomers with C_1 symmetry, which can be viewed as adding a B_2 unit off-plane to the B_8 ring, whereas that of $La_2B_{11}^-$ can be viewed as adding a B_3 unit in-plane to the B_8 ring in a second coordination shell. Chemical bonding analyses reveal localized B−B bonds on the edge of the clusters and delocalized bonds in the expanded boron frameworks. The interactions between the La atoms and the boron frameworks include the unique $(d-p)\delta$ bonding, which was found to be the key for inverse-sandwich complexes with monocyclic boron rings. The current study confirms that the largest monocyclic boron ring to form the inverse-sandwich structures is B_9 and provide insights into the structural evolutions of larger lanthanide boride clusters.

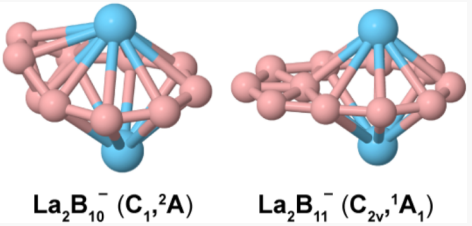

1. INTRODUCTION

Boron forms a wide range of important boride materials, from the superconducting MgB_2 and superhard transition-metal borides to borides with ultrahigh thermal conductivity.[1−6] Lanthanide (Ln) borides constitute another interesting class of boride materials with unique magnetic, optical, superconducting, mechanical, and thermoelectric properties.[7−10] Over the past two decades, the structures and chemical bonding of size-selected bare boron clusters have been studied by joint experimental and theoretical methods,[11−15] discovering planar clusters, nanotubular structures, graphene-like borophenes, and fullerene-like borospherenes.[15−22] Transition-metal-doped boron clusters have led to a new direction of boron nanoclusters, giving rise to new structures and bonding, such as the metal-centered aromatic borometallic wheels[23−25] and tubular metal-centered drums.[26−29] However, lanthanide boride clusters have been rarely explored until recently,[30−40] despite the importance of bulk lanthanide boride materials.

The PrB_7^- cluster represents the first lanthanide boride cluster characterized by photoelectron spectroscopy (PES) and quantum chemistry calculations.[32] It was found to have a half-sandwich structure with the Pr atom coordinated to a doubly aromatic bowl-shaped η-B_7^{3-} unit. A series of small lanthanide boride clusters, SmB_6^-, CeB_6^-, PrB_3^-, and PrB_4^-,[33−35] have been reported, which all have planar structures with the Ln atom on the edge. Most recently, larger lanthanide boride clusters have been studied, uncovering an inverse triple-decker and an interesting cage-like spherical trihedral metallo-borospherene.[36,37] Among all the lanthanide boride clusters, photoelectron spectra of the dilanthanide octaboron clusters ($Ln_2B_8^-$, Ln = La, Pr, Tb) were observed to be relatively simple and these clusters were found to consist of unprecedented inverse-sandwich structures with D_{8h} symmetry,[38] in which the two Ln atoms sandwiching the doubly aromatic B_8 monocyclic ring with strong $(d-p)\pi$ and $(d-p)\delta$ bonding between the Ln atoms and the B_8 ring. Subsequently, two more dilanthanide inverse-sandwich complexes, $La_2B_7^-$ and $La_2B_9^-$, were characterized, suggesting that there exists a class of such inverse-sandwich structures with different boron ring sizes.[39] An interesting question is can inverse-sandwiches be formed with larger B_x rings? What are the structures of the larger dilanthanide boride clusters ($La_2B_x^-$, $x \geq 10$)?

In this article we aim to answer these questions and report an investigation of $La_2B_{10}^-$ and $La_2B_{11}^-$ using PES and quantum calculations. Our global-minimum structural searches show that the most stable structure of $La_2B_{10}^-$ consists of a pair

Received: February 7, 2021
Revised: March 10, 2021
Published: March 19, 2021

https://doi.org/10.1021/acs.jpca.1c01149
J. Phys. Chem. A 2021, 125, 2622−2630

of chiral enantiomers (C_1, ^{1}A), which can be viewed as adding a B_2 unit off-plane to a La_2B_8 inverse sandwich. The global minimum of $La_2B_{11}^-$ is also based on the La_2B_8 inverse-sandwich structure, with the three extra B atoms being added to the B_8 ring in-plane by forming a second coordination shell and a perfectly planar expanded B_{11} framework. Chemical bonding analyses show localized B−B bonds on the edge and multicentered B−B bonds on the expanded boron frameworks. The expanded inverse sandwiches also feature the (d−p)δ bonding between the La atoms and the boron frameworks. The current study enriches the family of lanthanide inverse-sandwich clusters, providing insight into the formation and stability of larger lanthanide boride clusters.

2. METHODS

2.1. Photoelectron Spectroscopy. The experiments were carried out using a magnetic-bottle PES apparatus, coupled with a time-of-flight mass spectrometer and a laser vaporization cluster source, details of which have been published before.[12] Briefly, the lanthanide boride clusters were produced by laser vaporization of a disc target made from a mixed powder of La (Alfa Aesar, 99.9% purity) and B (Alfa Aesar, 96% ^{11}B enriched, 99.9% elemental purity) with a 5/2 La/B mass ratio. The laser-induced plasma was quenched by a He carrier gas seeded with 5% Ar inside the nozzle to initiate nucleation. The nascent clusters were entrained by the carrier gas and underwent a supersonic expansion to form a cold cluster beam. After passing a skimmer, negatively charged clusters were extracted from the collimated cluster beam and analyzed by a time-of-flight mass spectrometer. A range of $La_2B_x^-$ clusters were formed in the source. The $La_2B_{10}^-$ and $La_2B_{11}^-$ clusters of current interest were mass-selected and decelerated before being photodetached by the 193 nm radiation from an ArF excimer laser. As discussed previously,[12] the cluster temperatures depended on the resident time inside the nozzle. We usually selected clusters that had the longest resident time because they were colder. Photoelectrons were collected at nearly 100% efficiency by the magnetic bottle and analyzed in a 3.5 m long electron flight tube. Photoelectron spectra were calibrated using the known spectra of the Au^- and Bi^- atomic anions. The electron kinetic energy (KE) resolution of the PES apparatus (ΔKE/KE) was around 2.5%, that is, ~25 meV for 1 eV electrons.

2.2. Computational Methods. Unbiased structural searches for the global minima of $La_2B_{10}^-$ and $La_2B_{11}^-$ with different spin multiplicities were carried out using the TGMin 2.0 package,[41−43] combined with energy calculations using the ADF 2017.114 software.[44−46] In the structure search, the Perdew−Burke−Ernzerhof (PBE) generalized gradient approximation (GGA) density functional[47] and Slater-type basis sets with the triple-ζ plus one polarization function (TZP) were used.[48] The scalar relativistic effects were considered by the zero-order-regular approximation (ZORA).[49] All local minima were verified by calculations of the harmonic vibrational frequencies. Low-lying isomers were subsequently reoptimized using the hybrid PBE0 functional in Gaussian 16.[50] In the reoptimization calculations, the cc-pVTZ valence triple-ζ basis set was used for boron[51] and the Stuttgart energy-consistent relativistic pseudopotential ECP28MWB(La) with the corresponding ECP28MWB_ANO basis set for La.[52,53]

Photodetachment transitions were computed approximately using the ΔSCF-TDDFT approach.[54] The first vertical detachment energy (VDE_1) was calculated as the energy difference between the anion and the neutral at the anion geometry. Vertical excitation energies of the neutral species calculated using the time-dependent DFT method and the SAOP model (TD−SAOP) were added to VDE_1 to yield the higher VDEs.[55] The obtained VDEs were fitted with unit-area Gaussians of 0.15 eV width to produce a simulated spectrum. Chemical bonding was analyzed using the adaptive natural density partitioning (AdNDP)[56] using the PBE0/cc-pVTZ/ECP28MWB method based on the geometry at the same level from Gaussian 16. The charges of the atoms were calculated using various partition schemes.[57−61]

3. RESULTS

3.1. Photoelectron Spectroscopy. The photoelectron spectra of $La_2B_{10}^-$ and $La_2B_{11}^-$ at 193 nm (6.424 eV) are shown in Figures 1 and 2, respectively. The PES bands are

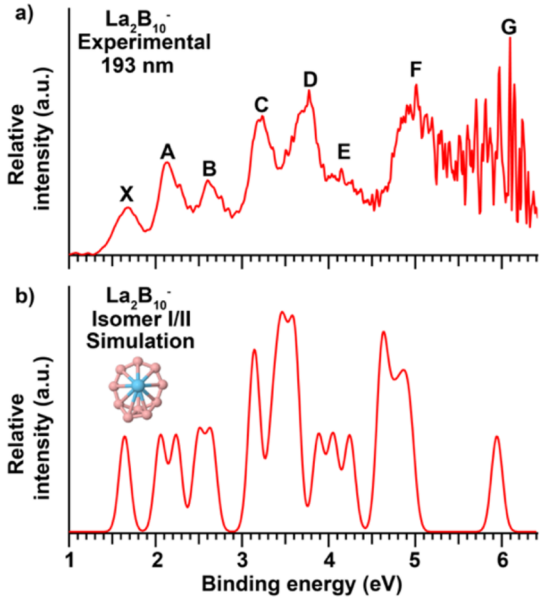

Figure 1. (a) Photoelectron spectrum of $La_2B_{10}^-$ at 193 nm (6.424 eV) and (b) simulated spectrum of the global minimum isomer I/II at the TD-SAOP/TZP level.

labeled with letters (X, A, B, ...), and the VDEs measured from the maxima of all the observed bands are given in Tables 1 and 2 for $La_2B_{10}^-$ and $La_2B_{11}^-$, respectively, where they are compared with the theoretical results.

The 193 nm spectrum of $La_2B_{10}^-$ shows seven well-resolved bands, labeled as X, A−F in Figure 1a. The lowest-binding-energy band (X) gives rise to the first VDE of 1.69 eV. The first adiabatic detachment energy (ADE) is estimated from the onset of band X as 1.48 eV, which also represents the electron affinity (EA) of the corresponding neutral La_2B_{10}. The next band A is observed at 2.14 eV followed by band B at 2.60 eV. Two intense bands, C and D, are observed at 3.23 and 3.77 eV, respectively. A broad and weaker band E appears at 4.15 eV, followed by a small energy gap and a broad band F at 5.01 eV. Beyond 5.5 eV, the signal-to-noise ratio becomes poor and a band G at ~6 eV is tentatively labeled for the sake of discussion. Unlike the previously reported spectra of the inverse-sandwich complexes $La_2B_x^-$ (x = 7−9),[38,39] the spectrum of $La_2B_{10}^-$ displays complicated and broad features, indicating a low symmetry structure.

https://doi.org/10.1021/acs.jpca.1c01149
J. Phys. Chem. A 2021, 125, 2622−2630

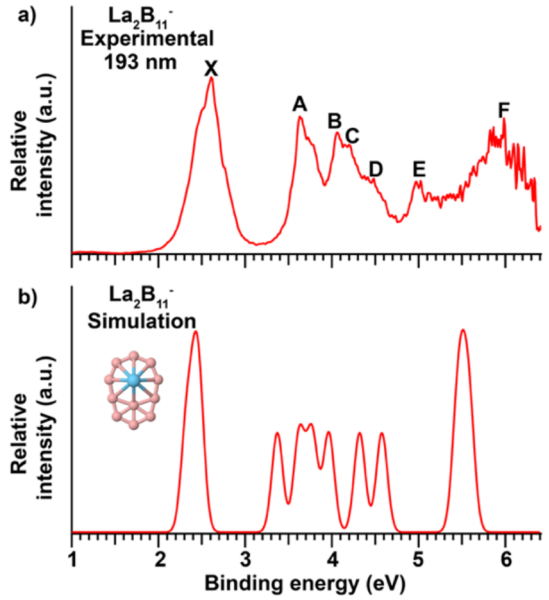

Figure 2. (a) Photoelectron spectra of $La_2B_{11}^-$ at 193 nm (6.424 eV) and (b) the simulated spectrum of the global minimum structure at the TD-SAOP/TZP level.

The 193 nm spectrum of $La_2B_{11}^-$ appears simpler than that of $La_2B_{10}^-$, displaying five major bands, as shown in Figure 2a. The most intense band X yields the first VDE at 2.61 eV, but its high relative intensity and large spectral width suggests that it likely contains multiple detachment channels. The first ADE, i.e., the EA of La_2B_{11}, is estimated from the onset of band X to be 2.27 eV, which is much higher than that of La_2B_{10}. Following a large energy gap, a well-resolved band A is observed at 3.63 eV. The next spectral feature is quite broad and three overlapping bands are discernible: band B at 4.06 eV, band C at 4.21 eV, and band D at 4.49 eV. A relatively weak band E at 4.98 eV is well resolved, following a small energy gap. A broad and strong band F at ~6.0 eV is observed at the high binding energy side, which probably contains multiple detachment channels.

3.2. Global Minima of $La_2B_{10}^-$ and $La_2B_{11}^-$. The optimized structures within 50 kcal/mol of the global minima of $La_2B_{10}^-$ and $La_2B_{11}^-$ are presented in Figures S1 and S2, respectively. All the structures were determined to be true minima without imaginary frequencies. We found that the global minimum of $La_2B_{10}^-$ consists of two degenerate expanded inverse-sandwich structures, I and II (C_1, ^2A), as shown in Figure 3. Interestingly, these two structures are a pair of chiral enantiomers. The top and bottom views for each enantiomer are shown in Figure 3, and the detailed bond lengths of each structure are given in Figure S3. These structures can be viewed as adding a B_2 unit *parallelly* above the B_8-ring plane of a $La_2B_8^-$ inverse sandwich. The B_2 unit distorts the local B_8 ring structure, creating a low-symmetry cluster (C_1) in which one La is coordinated by a B_8 ring on one side and the other La is coordinated by a B_9 ring on the other side of the inverse sandwich. The next low-lying isomer III (C_{2v}, $^2A_1$; Figure S4) is 3.24 kcal/mol at the PBE level (3.75 kcal/mol at the PBE0 level) higher in energy above the global minimum (Figure S1). Isomer III can be viewed as inserting a B_2 unit *perpendicularly* into the B_8-ring of a $La_2B_8^-$ inverse sandwich. This isomer has a higher symmetry (C_{2v}) and each La atom is coordinated by a B_9 ring.

The global minimum of $La_2B_{11}^-$ was found to have a closed-shell C_{2v} ($^1A_1$) inverse-sandwich structure, as shown in Figure 4. The structure can be viewed as a $La_2B_8^-$ inverse sandwich, where the additional three B atoms are added to the same plane as the B_8 ring in a second coordination shell. The

Table 1. Experimental Vertical Detachment Energies (VDEs) of $La_2B_{10}^-$ in Comparison with Theoretical VDEs Computed for the Global Minimum Structure I/II (C_1, ^2A) at the TD-SAOP/TZP Level (All Energies in eV)

feature	VDE (exp)[a]	final state and electronic configuration xs(SAOP)	VDE (theo)
X	1.69	^1A {...0.71a^{2}72a^{2}73a^{2}74a^{2}75a^{2}76a^{2}77a^{2}78a^{2}79a^{2}80a^{2}81a^{2}82a^2**83a^0**}	1.64
A	2.14	^3A {...0.71a^{2}72a^{2}73a^{2}74a^{2}75a^{2}76a^{2}77a^{2}78a^{2}79a^{2}80a^{2}81a^2**82a^1**83a^1}	2.06
		^1A {...0.71a^{2}72a^{2}73a^{2}74a^{2}75a^{2}76a^{2}77a^{2}78a^{2}79a^{2}80a^{2}81a^2**82a^1**83a^1}	2.24
B	2.60	^3A {...0.71a^{2}72a^{2}73a^{2}74a^{2}75a^{2}76a^{2}77a^{2}78a^{2}79a^{2}80a^2**81a^1**82a^{2}83a^1}	2.50
		^1A {...0.71a^{2}72a^{2}73a^{2}74a^{2}75a^{2}76a^{2}77a^{2}78a^{2}79a^{2}80a^2**81a^1**82a^{2}83a^1}	2.64
C	3.23	^3A {...0.71a^{2}72a^{2}73a^{2}74a^{2}75a^{2}76a^{2}77a^{2}78a^{2}79a^2**80a^1**81a^{2}82a^{2}83a^1}	3.12
		^3A {...0.71a^{2}72a^{2}73a^{2}74a^{2}75a^{2}76a^{2}77a^{2}78a^2**79a^1**80a^{2}81a^{2}82a^{2}83a^1}	3.16
		^1A {...0.71a^{2}72a^{2}73a^{2}74a^{2}75a^{2}76a^{2}77a^{2}78a^{2}79a^2**80a^1**81a^{2}82a^{2}83a^1}	3.35
D	3.77	^3A {...0.71a^{2}72a^{2}73a^{2}74a^{2}75a^{2}76a^{2}77a^2**78a^1**79a^{2}80a^{2}81a^{2}82a^{2}83a^1}	3.44
		^1A {...0.71a^{2}72a^{2}73a^{2}74a^{2}75a^{2}76a^{2}77a^{2}78a^2**79a^1**80a^{2}81a^{2}82a^{2}83a^1}	3.48
		^3A {...0.71a^{2}72a^{2}73a^{2}74a^{2}75a^{2}76a^2**77a^1**78a^{2}79a^{2}80a^{2}81a^{2}82a^{2}83a^1}	3.60
		^1A {...0.71a^{2}72a^{2}73a^{2}74a^{2}75a^{2}76a^{2}77a^2**78a^1**79a^{2}80a^{2}81a^{2}82a^{2}83a^1}	3.61
E	4.15	^1A {...0.71a^{2}72a^{2}73a^{2}74a^{2}75a^{2}76a^2**77a^1**78a^{2}79a^{2}80a^{2}81a^{2}82a^{2}83a^1}	3.88
		^3A {...0.71a^{2}72a^{2}73a^{2}74a^{2}75a^2**76a^1**77a^{2}78a^{2}79a^{2}80a^{2}81a^{2}82a^{2}83a^1}	4.05
		^1A {...0.71a^{2}72a^{2}73a^{2}74a^{2}75a^2**76a^1**77a^{2}78a^{2}79a^{2}80a^{2}81a^{2}82a^{2}83a^1}	4.24
F	5.01	^3A {...0.71a^{2}72a^{2}73a^{2}74a^2**75a^1**76a^{2}77a^{2}78a^{2}79a^{2}80a^{2}81a^{2}82a^{2}83a^1}	4.61
		^3A {...0.71a^{2}72a^{2}73a^2**74a^1**75a^{2}76a^{2}77a^{2}78a^{2}79a^{2}80a^{2}81a^{2}82a^{2}83a^1}	4.64
		^1A {...0.71a^{2}72a^{2}73a^{2}74a^2**75a^1**76a^{2}77a^{2}78a^{2}79a^{2}80a^{2}81a^{2}82a^{2}83a^1}	4.75
		^1A {...0.71a^{2}72a^{2}73a^2**74a^1**75a^{2}76a^{2}77a^{2}78a^{2}79a^{2}80a^{2}81a^{2}82a^{2}83a^1}	4.85
		^3A {...0.71a^{2}72a^2**73a^1**74a^{2}75a^{2}76a^{2}77a^{2}78a^{2}79a^{2}80a^{2}81a^{2}82a^{2}83a^1}	4.94
G	~6	^3A {...0.71a^2**72a^1**73a^{2}74a^{2}75a^{2}76a^{2}77a^{2}78a^{2}79a^{2}80a^{2}81a^{2}82a^{2}83a^1}	5.94

[a]The experimental uncertainty was estimated to be ±0.03 eV.

https://doi.org/10.1021/acs.jpca.1c01149
J. Phys. Chem. A 2021, 125, 2622−2630

Table 2. Experimental Vertical Detachment Energies (VDEs) of $La_2B_{11}^-$ in Comparison with Theoretical VDEs Computed from the Global Minimum Structure (C_{2v}, $^1A_1$) at the TD-SAOP/TZP Level (All Energies in eV)

feature	VDE (exp)[a]	final state and electronic configuration (SAOP)	VDE (theo)
X	2.61	$^2B_1$ {...0.32$a_1^2$20$b_2^2$16$b_1^2$17$b_1^2$18$b_1^2$33$a_1^2$21$b_2^2$34$a_1^2$9$a_2^2$10$a_2^2$22b_2^2**19b_1^1**}	2.32
		$^2B_2$ {...0.32$a_1^2$20$b_2^2$16$b_1^2$17$b_1^2$18$b_1^2$33$a_1^2$21$b_2^2$34$a_1^2$9$a_2^2$10a_2^2**22b_2^1**19b_1^2}	2.42
		$^2A_2$ {...0.32$a_1^2$20$b_2^2$16$b_1^2$17$b_1^2$18$b_1^2$33$a_1^2$21$b_2^2$34$a_1^2$9a_2^2**10a_2^1**22$b_2^2$19b_1^2}	2.47
A	3.63	$^2A_2$ {...0.32$a_1^2$20$b_2^2$16$b_1^2$17$b_1^2$18$b_1^2$33$a_1^2$21$b_2^2$34a_1^2**9a_2^1**10$a_2^2$22$b_2^2$19b_1^2}	3.37
B	4.06	$^2A_1$ {...0.32$a_1^2$20$b_2^2$16$b_1^2$17$b_1^2$18$b_1^2$33$a_1^2$21b_2^2**34a_1^1**9$a_2^2$10$a_2^2$22$b_2^2$19b_1^2}	3.62
C	4.21	$^2B_2$ {...0.32$a_1^2$20$b_2^2$16$b_1^2$17$b_1^2$18$b_1^2$33a_1^2**21b_2^1**34$a_1^2$9$a_2^2$10$a_2^2$22$b_2^2$19b_1^2}	3.77
D	4.49	$^2A_1$ {...0.32$a_1^2$20$b_2^2$16$b_1^2$17$b_1^2$18b_1^2**33a_1^1**21$b_2^2$34$a_1^2$9$a_2^2$10$a_2^2$22$b_2^2$19b_1^2}	3.97
E	4.98	$^2B_1$ {...0.32$a_1^2$20$b_2^2$16$b_1^2$17b_1^2**18b_1^1**33$a_1^2$21$b_2^2$34$a_1^2$9$a_2^2$10$a_2^2$22$b_2^2$19b_1^2}	4.32
		$^2B_1$ {...0.32$a_1^2$20$b_2^2$16b_1^2**17b_1^1**18$b_1^2$33$a_1^2$21$b_2^2$34$a_1^2$9$a_2^2$10$a_2^2$22$b_2^2$19b_1^2}	4.58
F	~6.0	$^2B_1$ {...0.32$a_1^2$20b_2^2**16b_1^1**17$b_1^2$18$b_1^2$33$a_1^2$21$b_2^2$34$a_1^2$9$a_2^2$10$a_2^2$22$b_2^2$19b_1^2}	5.45
		$^2B_2$ {...0.32a_1^2**20b_2^1**16$b_1^2$17$b_1^2$18$b_1^2$33$a_1^2$21$b_2^2$34$a_1^2$9$a_2^2$10$a_2^2$22$b_2^2$19b_1^2}	5.52
		$^2A_1$ {...**32a_1^1**20$b_2^2$16$b_1^2$17$b_1^2$18$b_1^2$33$a_1^2$21$b_2^2$34$a_1^2$9$a_2^2$10$a_2^2$22$b_2^2$19b_1^2}	5.59

[a]The experimental uncertainty was estimated to be ±0.03 eV.

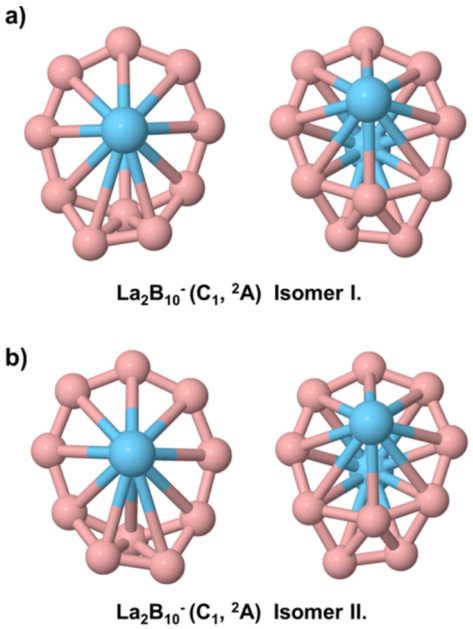

Figure 3. Top and bottom views of the two enantiomers of the chiral global minimum of $La_2B_{10}^-$.

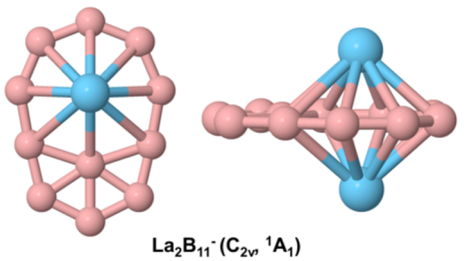

Figure 4. Top and side views of the optimized global minimum structure of $La_2B_{11}^-$.

detailed bond lengths of the global minimum are shown in Figure S5. The nearest low-lying isomer II (Figure S2) has C_1 symmetry and it is 8.86 kcal/mol (at the PBE/TZP level) and 11.96 kcal/mol (at the PBE0/TZP level) higher in energy than the global minimum, suggesting the high stability of the C_{2v} $La_2B_{11}^-$ inverse-sandwich structure.

To validate the global minimum structures of $La_2B_{10}^-$ and $La_2B_{11}^-$, we have calculated their VDEs, as compared with the experimental data in Tables 1 and 2, as well as in Figures 1b and 2b, respectively, at the TD-SAOP/TZP level. Because isomer III of $La_2B_{10}^-$ is relatively low-lying, we also computed its VDEs (Table S1) and compared its simulated spectrum with the experiment (Figure S6). The VDE_1 and ADE values for the chiral global minimum of $La_2B_{10}^-$ and the C_{2v} global minimum of $La_2B_{11}^-$ were computed at different levels of theory, as summarized in Table S2. The atomic charges for isomers I/II and III of $La_2B_{10}^-$ and that of isomer I of $La_2B_{11}^-$ are given in Tables S3 and S4, respectively. The coordinates for isomers I/II and III of $La_2B_{10}^-$ and that of isomer I of $La_2B_{11}^-$ at the PBE0 level are given in Table S5. Except for their structures, the chiral global minimum isomers I/II of $La_2B_{10}^-$ have identical electronic structure and chemical bonding properties.

4. DISCUSSION

4.1. Comparison between Experiment and Theory. As shown in Table S2, both PBE and PBE0 functionals in general gave similar VDE_1 and ADE values for the global minima of $La_2B_{10}^-$ and $La_2B_{11}^-$, both in good agreement with the experimental data. Each computed VDE at the TD-SAOP/TZP level for the global minima is fitted with a Gaussian function of unit area and a width of 0.15 eV to produce the simulated spectra, which are compared with the experimental data in Figures 1b and 2b for $La_2B_{10}^-$ and $La_2B_{11}^-$, respectively.

4.1.1. $La_2B_{10}^-$. The global minimum chiral structure of $La_2B_{10}^-$ has a doublet ground state (^2A) with a single electron in the 83a orbital (SOMO, Figure S7a). The computed VDE_1/ADE of 1.67/1.48 eV at the PBE/TZP level (Table S2) by removing the electron from the SOMO are in excellent agreement with the experimental data of 1.69/1.48 eV. The removal of an electron from the HOMO (82a, Figure S7a) gives rise to two final spin states, one triplet state with a computed VDE of 2.06 eV and one singlet state with a computed VDE of 2.24 eV; both are consistent with the observed band A at 2.14 eV (Table 1). Similarly, detachment from the HOMO−1 (81a) yields a triplet state with a computed VDE at 2.50 eV and a singlet state at 2.64 eV, both matching well with the observed band B at 2.60 eV (Table 1). Band C at 3.23 eV and band D at 3.77 eV contain multiple

https://doi.org/10.1021/acs.jpca.1c01149
J. Phys. Chem. A 2021, 125, 2622−2630

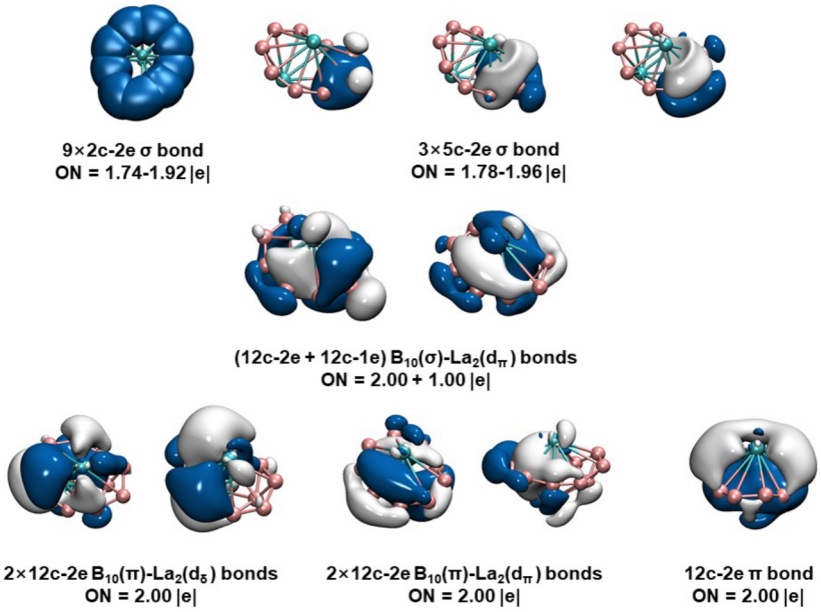

Figure 5. AdNDP analyses of the global minimum C_1 chiral structure of $La_2B_{10}^-$ at the PBE0/VTZ level.

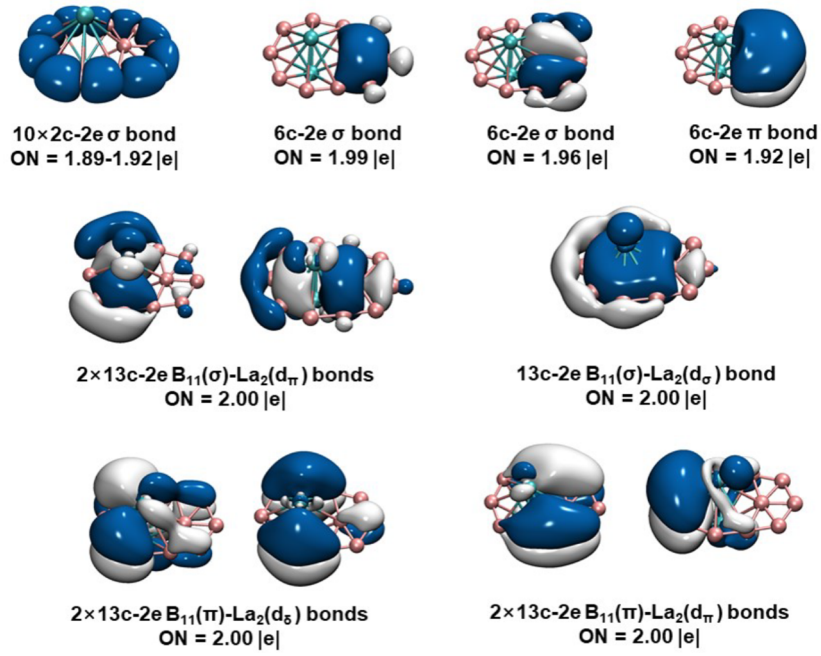

Figure 6. AdNDP analyses of the global minimum C_{2v} structure of $La_2B_{11}^-$ at the PBE0/VTZ level.

detachment channels from the HOMO−2 (80a), HOMO−3 (79a), HOMO−4 (78a), and HOMO−5 (77a), while band E at 4.15 eV agrees well with the computed VDEs from the HOMO−6 (76a). Band F is quite broad and in good agreement with detachment channels from the HOMO−7 (75a), HOMO−8 (74a) and HOMO−9 (73a), while the tentative band G can be explained by detachment from the 72a orbital (Table 1). The simulated spectrum of the C_1 chiral structure of $La_2B_{10}^-$ reproduces well the experimental features (Figure 1b). On the other hand, the low-lying isomer III gives rises to a relatively simple simulated spectral pattern due to its higher symmetry, which does not agree with the experiment, as shown in Figure S6. Thus, the good agreement between the experimental and theoretical data provides strong evidence for the chiral C_1 structure as the global minimum of $La_2B_{10}^-$.

4.1.2. $La_2B_{11}^-$. The global minimum of $La_2B_{11}^-$ (Figure 4) is closed shell ($^1A_1$). Thus, electron detachment from each occupied orbital yields a single doublet final state (Table 2). The computed VDE_1/ADE values of 2.34/2.23 eV at the PBE/TZP level (Table S2) are in reasonable agreement with the experimental values of 2.67/2.27 eV. The larger discrepancy between the computed VDE_1 and the experimental VDE_1 is due to the fact that the first real detachment channel at a lower VDE is not resolved in the broad band X in the 193 nm spectrum, as can be seen by the shoulder on the lower binding energy side of band X (Figure 2a). The X band is consistent with the first three detachment channels from the HOMO

https://doi.org/10.1021/acs.jpca.1c01149
J. Phys. Chem. A 2021, 125, 2622−2630

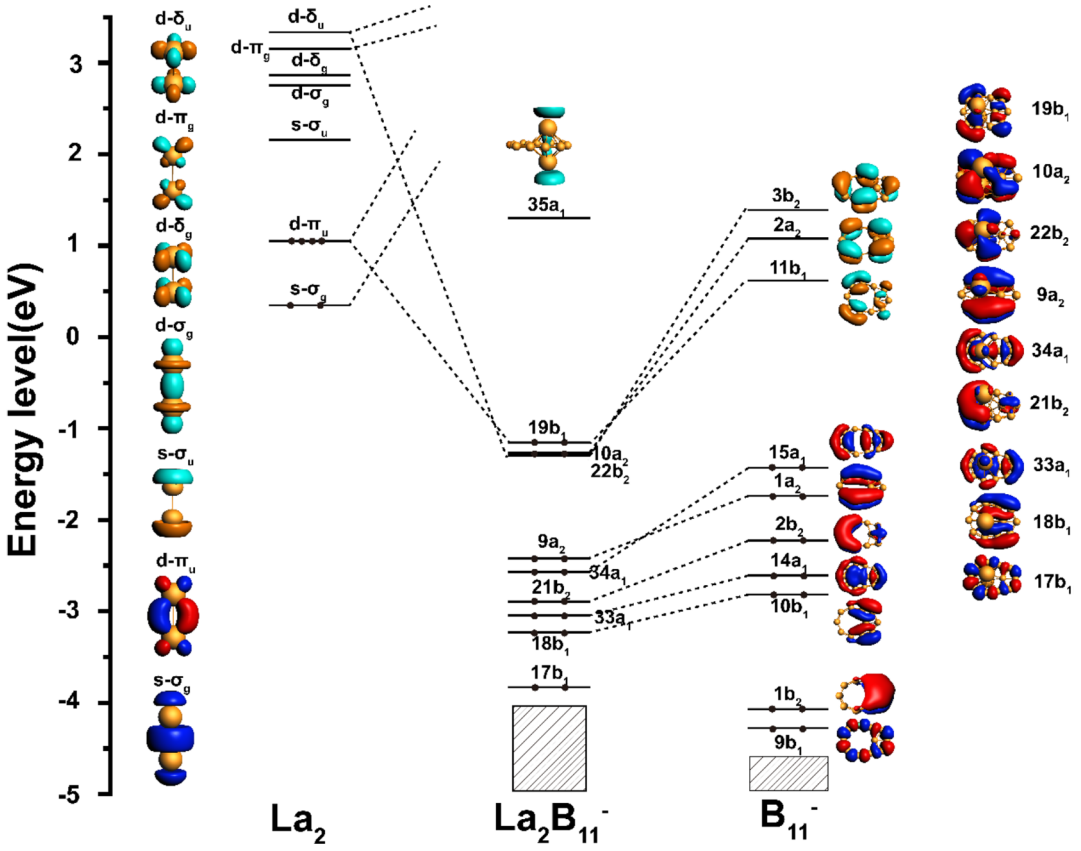

Figure 7. MO bonding scheme of the C_{2v} global minimum of $La_2B_{11}^-$ at the level of PBE0/TZP, illustrating the bonding interactions between the La···La and B_{11}^- framework (isovalue = 0.03 au).

($19b_1$), HOMO−1 ($22b_2$), and HOMO−2 ($10a_2$) (Table 2), which give rise to closely spaced VDEs. Electron removal from the HOMO−3 ($9a_2$), HOMO−4 ($34a_1$), HOMO−5 ($21b_2$), and HOMO−6 ($33a_1$) results in four closely spaced detachment channels with computed VDEs ranging from 3.37 to 3.97 eV, which agree well with bands A, B, C, D, respectively (Table 2). These are followed by two detachment channels from the HOMO−7 ($18b_1$) and HOMO−8 ($17b_1$) with computed VDEs of 4.32 and 4.58 eV, which can be assigned to the broad band E. The next three detachment channels from the HOMO−9 ($16b_1$), HOMO−10 ($20b_2$), and HOMO−11 ($32a_1$) give rise to three closely spaced VDEs from 5.45 to 5.59 eV (Table 2), consistent with the broad band F at the high binding energy side (Figure 2). The overall spectral pattern of the simulated spectrum agrees well with the experiment (Figure 2), confirming the inverse-sandwich C_{2v} structure to be the global minimum of $La_2B_{11}^-$.

4.2. Chemical Bonding Analyses. The low-symmetry structures, in particular the C_1 global minimum of $La_2B_{10}^-$, make it a challenge to decipher the chemical bonding in the two large dilanthanum boride clusters. Because of the electron deficiency of the B atom, multicenter bonding is prevalent in boron clusters.[62−64] In general, for the dilanthanide inverse sandwiches the B 2s and in-plane 2p orbitals form the σ-bonding network, while the two Ln atoms form symmetric and antisymmetric σ (d_{z^2}), π (d_{xz}, d_{yz}) and δ ($d_{x^2-y^2}$, d_{xy}) type d-orbital pairs that can interact with the out-of-plane B 2p orbitals of the ring via (d−p)σ, (d−p)π, and (d−p)δ bonds.[38−40] The canonical Kohn−Sham molecular orbitals of isomers I/II and III of $La_2B_{10}^-$ and isomer I of $La_2B_{11}^-$ are shown in Figure S7. To better understand the chemical bonding and stability of the global minima of $La_2B_{10}^-$ and $La_2B_{11}^-$, we performed AdNDP analyses,[56] as shown in Figures 5 and 6, respectively. Because of the complexity of the bonding, we also did AdNDP analyses for the B_{10}^- and B_{11}^- frameworks or ligands without the La atoms, as shown in Figures S8 and S9.

4.2.1. $La_2B_{10}^-$. The AdNDP result for the B_{10}^- framework (Figure S8a) of the chiral global minimum of $La_2B_{10}^-$ exhibit nine B−B two-center two-electron (2c−2e) bonds on the periphery, three 5c−2e delocalized bonds over the expanded part of the B_{10} framework. The remaining 7 electrons form four totally delocalized σ and π bonds over the entire B_{10} framework, which have orbital interactions with the two La atoms. Indeed, upon coordination with the La···La atoms in the chiral $La_2B_{10}^-$, the nine 2c−2e bonds and the three 5c−2e bonds are largely unchanged (Figure 5). Six 12c−2e bonds and one 12c−1e bond are observed, suggesting that three unoccupied MOs in the B_{10} framework are stabilized significantly via metal−ligand interactions, so that the B_{10}^- ligand can be viewed to have gained 6 electrons in $La_2B_{10}^-$. Since the extra unpaired electron remains largely in a La-based orbital, the two La atoms can be viewed as having oxidation states of La(III) and La(II) in $La_2B_{10}^-$. The charge transfer from the La···La atoms to the B_{10}^- framework is consistent with the charge population analyses (Table S3). The six 12c−2e bonds are formed from the interactions between the La···La $5d_\sigma$, $5d_\pi$, and $5d_\delta$ orbitals and the B_{10}^- ligand. The two 12c−2e (d−p)δ bonds due to the interactions of the La $5d_\delta$ orbitals and the π orbitals of the boron framework are particularly

https://doi.org/10.1021/acs.jpca.1c01149
J. Phys. Chem. A 2021, 125, 2622−2630

interesting. Similar (d−p)δ bonds have been shown previously to play critical roles in stabilizing the monocyclic inverse-sandwich structures in $La_2B_x^-$ (x = 7−9).[38−40]

The AdNDP results for the low-lying C_{2v} isomer III of $La_2B_{10}^-$ (Figure S10 and Figure S8b for the B_{10}^- ligand) are similar to that of the chiral global minimum, but the bonding is easier to visualize due to the higher symmetry of the C_{2v} isomer. One notable difference is the number of 2c−2e B−B bonds on the periphery of the two structures: nine in the C_1 global minimum vs seven in the C_{2v} isomer. Presumably the more B−B 2c−2e σ-bonds in the C_1 structures makes it more stable because the localized B−B bonds are stronger bonds than the multicentered bonds.

4.2.2. $La_2B_{11}^-$. The higher symmetry of the $La_2B_{11}^-$ global minimum and its planar boron framework make it easier to visualize its bonding. The AdNDP analyses of the planar B_{11}^- framework (Figure S9) reveal ten 2c−2e B−B σ bonds on the periphery, three 6c−2e bonds (one π bond and two σ bonds) involving the second and first coordination shells, and four totally delocalized 11c−2e bonds (two π bonds and two σ bonds). The three π bonds fulfill the $4N + 2$ Hückel rule, indicating that the B_{11}^- ligand is π-aromatic. Upon complexation to the two La···La atoms, the 2c−2e bonds and the 6c−2e bonds essentially remain the same while the 11c−2e bonds interact with the La atoms, as shown in Figure 6. There are seven delocalized 13c−2e bonds representing interactions between the La···La $5d_\sigma$, $5d_\pi$, and $5d_\delta$ orbitals and the B_{11}^- ligand. The seven 13c−2e bonds suggest that three unoccupied MOs of the B_{11}^- ligands are also involved in bonding with the La···La atoms and are significantly stabilized, as shown in Figure 7. Two of these MOs are π MOs ($3b_2$ and $2a_2$ in Figure 7), which form the two 13c−2e (d−p)δ bonds; one of these MOs ($11b_1$ in Figure 7) forms a 13c−2e (d−p)π bond. Thus, the B_{11}^- ligand can be viewed as gaining six electrons upon complexation with the two La···La atoms, indicating that the La atoms are in their stable La(III) oxidation state in $La_2B_{11}^-$, consistent with charge population analyses (Table S4). Figure 7 also shows that the $La_2B_{11}^-$ cluster has an extremely stable closed-shell electron configuration with 40 valence electrons and a large HOMO−LUMO gap. Such a stable electronic structure is evidenced by the very high ADE of $La_2B_{11}^-$ (2.27 eV) relative to that of $La_2B_{10}^-$ (1.48 eV). In fact, the bonding in $La_2B_{11}^-$ closely resemble that in the monocyclic $La_2B_9^-$ system,[39,40] again confirming the importance of the (d−p)δ bonds in stabilizing the inverse-sandwich structure.

4.3. Comparison with the Monocyclic $La_2B_x^-$ (x = 7−9) Systems. The structures of $La_2B_{10}^-$ and $La_2B_{11}^-$ confirm that for dilanthanide boride clusters ($Ln_2B_x^-$) the largest monocyclic ring (B_x) to form the inverse-sandwich structure in the 9-membered ring in $Ln_2B_9^-$.[39,40] Clearly, larger rings would reduce the orbital overlaps between the Ln···Ln atoms and the boron rings. Thus, for $Ln_2B_x^-$ clusters with x > 9, the additional boron atoms do not expand the ring size. Although $La_2B_9^-$ has a higher stability than $La_2B_8^-$ due to the fully occupied (d−p)δ bonding orbitals,[39,40] the $La_2B_{10}^-$ and $La_2B_{11}^-$ clusters are mainly based on a B_8-ring system. This can be understood readily from the fact that the B_8 ring size in the B_{11} framework in $La_2B_{11}^-$ is larger than the bare monocyclic B_8 ring in the $La_2B_8^-$ inverse sandwich because the B−B bond lengths for the two B atoms that are bonded to the second coordination shell are longer (Figure S5). This is consistent with the fact that the B_9 monocyclic ring is the largest size to form inverse sandwiches in dilanthanide boride clusters. It is conceivable that larger ring sizes may be possible for diactinide boride inverse-sandwich clusters due to the larger sizes of the actinide elements.

5. CONCLUSIONS

In conclusion, we report a joint photoelectron spectroscopy and quantum chemical study of two new inverse-sandwich complexes, $La_2B_{10}^-$ and $La_2B_{11}^-$. The global minimum structure of $La_2B_{10}^-$ is found to be chiral (C_1, ^2A) with an expanded inverse-sandwich structure, which can be viewed as adding a B_2 unit off-plane parallelly to the B_8 ring in a $La_2B_8^-$ inverse-sandwich cluster. The global minimum of $La_2B_{11}^-$ also has an expanded inverse-sandwich structure with a planar B_{11} framework, which can be viewed as adding three boron atoms to a B_8 ring as the second coordination shell. Chemical bonding analyses show that the expanded $La_2B_{10}^-$ and $La_2B_{11}^-$ inverse sandwiches have similar bonding as that in the monocyclic ring inverse sandwiches of $Ln_2B_x^-$ (x = 7−9), in which unique (d−p)δ bonding between the Ln···Ln atoms and the π orbitals on the boron rings was critical to stabilize the inverse-sandwich structures. The $La_2B_{11}^-$ cluster is found to have an exceptionally stable electron configuration with a large HOMO−LUMO gap and very high electron binding energy. The current study confirms that the largest monocyclic boron ring to form inverse sandwiches in dilanthanide boride clusters ($Ln_2B_x^-$) is nine. The $La_2B_{10}^-$ and $La_2B_{11}^-$ clusters enrich the family of inverse-sandwich complexes and provide insight into the structural evolution of larger lanthanide boride clusters.

■ ASSOCIATED CONTENT

Supporting Information

The Supporting Information is available free of charge at https://pubs.acs.org/doi/10.1021/acs.jpca.1c01149.

Low-lying isomers of $La_2B_{10}^-$ and $La_2B_{11}^-$, structural parameters and molecular orbitals of the global minima, comparison of simulated spectra, additional bonding analyses and theoretical VDEs, ADEs, and atomic charges, and Cartesian coordinates (PDF)

■ AUTHOR INFORMATION

Corresponding Authors

Wan-Lu Li − *Department of Chemistry and Key Laboratory of Organic Optoelectronics & Molecular Engineering of Ministry of Education, Tsinghua University, Beijing 100084, China*; Email: wanluli0716@gmail.com

Jun Li − *Department of Chemistry and Key Laboratory of Organic Optoelectronics & Molecular Engineering of Ministry of Education, Tsinghua University, Beijing 100084, China; Department of Chemistry, Southern University of Science and Technology, Shenzhen 518055, China*; orcid.org/0000-0002-8456-3980; Email: junli@tsinghua.edu.cn

Lai-Sheng Wang − *Department of Chemistry, Brown University, Providence, Rhode Island 02912, United States*; orcid.org/0000-0003-1816-5738; Email: lai-sheng_wang@brown.edu

Authors

Zhi-Yu Jiang − *Department of Chemistry and Key Laboratory of Organic Optoelectronics & Molecular Engineering of Ministry of Education, Tsinghua University, Beijing 100084, China*

https://doi.org/10.1021/acs.jpca.1c01149
J. Phys. Chem. A 2021, 125, 2622−2630

Teng-Teng Chen − *Department of Chemistry, Brown University, Providence, Rhode Island 02912, United States;* orcid.org/0000-0001-9480-615X

Wei-Jia Chen − *Department of Chemistry, Brown University, Providence, Rhode Island 02912, United States*

Complete contact information is available at: https://pubs.acs.org/10.1021/acs.jpca.1c01149

Author Contributions

#Z.Y.J. and T.T.C. contributed equally to this work.

Notes

The authors declare no competing financial interest.

■ ACKNOWLEDGMENTS

The experiment done at Brown University was supported by the National Science Foundation (CHE-1763380). The theoretical work done at Tsinghua University was supported by the National Natural Science Foundation of China (22033005). The calculations were done using supercomputers at the Southern University of Science and Technology (SUSTech) and Tsinghua National Laboratory for Information Science and Technology. The support of Guangdong Provincial Key Laboratory of Catalysis (No. 2020B121201002) is also acknowledged.

■ REFERENCES

(1) Nagamatsu, J.; Nakagawa, N.; Muranaka, T.; Zenitani, Y.; Akimitsu, J. Superconductivity at 39 K in magnesium diboride. *Nature* **2001**, *410*, 63−64.

(2) Chung, H. Y.; Weinberger, M. B.; Levine, J. B.; Kavner, A.; Yang, J.-M.; Tolbert, S. H.; Kaner, R. B. Synthesis of ultra-incompressible superhard rhenium diboride at ambient pressure. *Science* **2007**, *316*, 436−439.

(3) Kang, J. S.; Li, M.; Wu, H.; Nguyen, H.; Hu, Y. Experimental observation of high thermal conductivity in boron arsenide. *Science* **2018**, *361*, 575−578.

(4) Li, S.; Zheng, Q.; Lv, Y.; Liu, X.; Wang, X.; Huang, P. Y.; Cahill, D. G.; Lv, B. High thermal conductivity in cubic boron arsenide crystals. *Science* **2018**, *361*, 579−581.

(5) Tian, F.; Song, B.; Chen, X.; Ravichandran, N. K.; Lv, Y.; Chen, K.; Sullivan, S.; Kim, J.; Zhou, Y.; Liu, T.-H.; et al. Unusual high thermal conductivity in boron arsenide bulk crystals. *Science* **2018**, *361*, 582−585.

(6) Tian, F.; Ren, Z. High thermal conductivity in boron arsenide: from prediction to reality. *Angew. Chem., Int. Ed.* **2019**, *58*, 5824−5831.

(7) Carenco, S.; Portehault, D.; Boissiere, C.; Mezailles, N.; Sanchez, C. Nanoscaled metal borides and phosphides: recent developments and perspectives. *Chem. Rev.* **2013**, *113*, 7981−8065.

(8) Sussardi, A.; Tanaka, T.; Khan, A. U.; Schlapbach, L.; Mori, T. Enhanced thermoelectric properties of samarium boride. *J. Materiomics* **2015**, *1*, 196−204.

(9) Akopov, G.; Yeung, M. T.; Kaner, R. B. Rediscovering the crystal chemistry of borides. *Adv. Mater.* **2017**, *29*, 1604506.

(10) Scheifers, J. P.; Zhang, Y.; Fokwa, B. P. T. Boron: enabling exciting metal-rich structures and magnetic properties. *Acc. Chem. Res.* **2017**, *50*, 2317−2325.

(11) Alexandrova, A. N.; Boldyrev, A. I.; Zhai, H. J.; Wang, L. S. All-boron aromatic clusters as potential new inorganic ligands and building blocks in chemistry. *Coord. Chem. Rev.* **2006**, *250*, 2811−2866.

(12) Wang, L. S. Photoelectron spectroscopy of size-selected boron clusters: from planar structures to borophenes and borospherenes. *Int. Rev. Phys. Chem.* **2016**, *35*, 69−142.

(13) Li, W. L.; Chen, X.; Jian, T.; Chen, T. T.; Li, J.; Wang, L. S. From planar boron clusters to borophenes and metalloborophenes. *Nat. Rev. Chem.* **2017**, *1*, 0071.

(14) Pan, S.; Barroso, J.; Jalife, S.; Heine, T.; Asmis, K. R.; Meirno, G. Fluxional boron clusters: from theory to reality. *Acc. Chem. Res.* **2019**, *52*, 2732−2744.

(15) Jian, T.; Chen, X.; Li, S. D.; Boldyrev, A. I.; Li, J.; Wang, L. S. Probing the structures and bonding of size-selected boron and doped-boron clusters. *Chem. Soc. Rev.* **2019**, *48*, 3550−3591.

(16) Kiran, B.; Bulusu, S.; Zhai, H. J.; Yoo, S.; Zeng, X. C.; Wang, L. S. Planar-to-tubular structural transition in boron clusters: B_{20} as the embryo of single-walled boron nanotubes. *Proc. Natl. Acad. Sci. U. S. A.* **2005**, *102*, 961−964.

(17) Oger, E.; Crawford, N. R.; Kelting, R.; Weis, P.; Kappes, M. M.; Ahlrichs, R. Boron cluster cations: transition from planar to cylindrical structures. *Angew. Chem., Int. Ed.* **2007**, *46*, 8503−8506.

(18) Piazza, Z. A.; Hu, H. S.; Li, W. L.; Zhao, Y. F.; Li, J.; Wang, L. S. Planar hexagonal B_{36} as a potential basis for extended single-atom layer boron sheets. *Nat. Commun.* **2014**, *5*, 3113.

(19) Li, W. L.; Chen, Q.; Tian, W. J.; Bai, H.; Zhao, Y. F.; Hu, H. S.; Li, J.; Zhai, H. J.; Li, S. D.; Wang, L. S. The B_{35} cluster with a double-hexagonal vacancy: a new and more flexible structural motif for borophene. *J. Am. Chem. Soc.* **2014**, *136*, 12257−12260.

(20) Bai, H.; Chen, T. T.; Chen, Q.; Zhao, X. Y.; Zhang, Y. Y.; Chen, W. J.; Li, W. L.; Cheung, L. F.; Bai, B.; Cavanagh, J.; et al. Planar B_{41}^- and B_{42}^- clusters with double-hexagonal vacancies. *Nanoscale* **2019**, *11*, 23286−23295.

(21) Zhai, H. J.; Zhao, Y. F.; Li, W. L.; Chen, Q.; Bai, H.; Hu, H. S.; Piazza, Z. A.; Tian, W. J.; Lu, H. G.; Wu, Y. B.; et al. Observation of an all-boron fullerene. *Nat. Chem.* **2014**, *6*, 727−731.

(22) Chen, Q.; Li, W. L.; Zhao, Y. F.; Zhang, S. Y.; Hu, H. S.; Bai, H.; Li, H. R.; Tian, W. J.; Lu, H. G.; Zhai, H. J.; et al. Experimental and theoretical evidence of an axially chiral borospherene. *ACS Nano* **2015**, *9*, 754−760.

(23) Romanescu, C.; Galeev, T. R.; Li, W. L.; Boldyrev, A. I.; Wang, L. S. Aromatic metal-centered monocyclic boron rings: $Co©B_8^-$ and $Ru©B_9^-$. *Angew. Chem., Int. Ed.* **2011**, *50*, 9334−9337.

(24) Galeev, T. R.; Romanescu, C.; Li, W. L.; Wang, L. S.; Boldyrev, A. I. Observation of the highest coordination number in planar species: decacoordinated $Ta©B_{10}^-$ and $Nb©B_{10}^-$ anions. *Angew. Chem., Int. Ed.* **2012**, *51*, 2101−2105.

(25) Romanescu, C.; Galeev, T. R.; Li, W. L.; Boldyrev, A. I.; Wang, L. S. Transition-metal-centered monocyclic boron wheel clusters ($M©B_n$): a new class of aromatic borometallic compounds. *Acc. Chem. Res.* **2013**, *46*, 350−358.

(26) Popov, I. A.; Jian, J.; Lopez, G. V.; Boldyrev, A. I.; Wang, L. S. Cobalt-centered boron molecular drums with the highest coordination number in the CoB_{16}^- cluster. *Nat. Commun.* **2015**, *6*, 8654.

(27) Jian, T.; Li, W. L.; Chen, X.; Chen, T. T.; Lopez, G. V.; Li, J.; Wang, L. S. Competition between drum and quasi-planar structures in RhB_{18}^-: motifs for metallo-boronanotubes and metallo-borophenes. *Chem. Sci.* **2016**, *7*, 7020−7027.

(28) Jian, T.; Li, W. L.; Popov, I. A.; Lopez, G. V.; Chen, X.; Boldyrev, A. I.; Li, J.; Wang, L. S. Manganese-centered tubular boron cluster-MnB_{16}^-: a new class of transition-metal molecules. *J. Chem. Phys.* **2016**, *144*, 154310.

(29) Li, W. L.; Jian, T.; Chen, X.; Li, H. R.; Chen, T. T.; Luo, X. M.; Li, S. D.; Li, J.; Wang, L. S. Observation of a metal-centered B_2-Ta@B_{18}^- tubular molecular rotor and a perfect Ta@B_{20}^- boron drum with the record coordination number of twenty. *Chem. Commun.* **2017**, *53*, 1587−1590.

(30) Cheng, S.-B.; Berkdemir, C.; Castleman, A. Observation of d-p hybridized aromaticity in lanthanum-doped boron clusters. *Phys. Chem. Chem. Phys.* **2014**, *16*, 533−539.

(31) Cheng, S.-B.; Berkdemir, C.; Castleman, A. W. Mimicking the magnetic properties of rare earth elements using superatoms. *Proc. Natl. Acad. Sci. U. S. A.* **2015**, *112*, 4941−4945.

(32) Chen, T. T.; Li, W. L.; Jian, T.; Chen, X.; Li, J.; Wang, L. S. PrB_7^-: a praseodymium-doped boron cluster with a Pr^{II} center

coordinated by a doubly aromatic planar η^7-B_7^{3-} Ligand. *Angew. Chem., Int. Ed.* **2017**, *56*, 6916−6920.
(33) Robinson, P. J.; Zhang, X.; McQueen, T.; Bowen, K. H.; Alexandrova, A. N. SmB_6^- cluster anion: covalency involving f orbitals. *J. Phys. Chem. A* **2017**, *121*, 1849−1854.
(34) Chen, X.; Chen, T. T.; Li, W. L.; Lu, J. B.; Zhao, L. J.; Jian, T.; Hu, H. S.; Wang, L. S.; Li, J. Lanthanides with unusually low oxidation states in the PrB_3^- and PrB_4^- boride clusters. *Inorg. Chem.* **2019**, *58*, 411−418.
(35) Mason, J. L.; Harb, H.; Huizenga, C. D.; Ewigleben, J. C.; Topolski, J. E.; Hratchian, H. P.; Jarrold, C. C. Electronic and molecular structures of the CeB_6 monomer. *J. Phys. Chem. A* **2019**, *123*, 2040−2048.
(36) Chen, T. T.; Li, W. L.; Chen, W. J.; Li, J.; Wang, L. S. $La_3B_{14}^-$: an inverse triple-decker lanthanide boron cluster. *Chem. Commun.* **2019**, *55*, 7864−7867.
(37) Chen, T. T.; Li, W. L.; Chen, W. J.; Yu, X. H.; Dong, X. R.; Li, J.; Wang, L. S. Spherical trihedral metallo-borospherenes. *Nat. Commun.* **2020**, *11*, 2766.
(38) Li, W. L.; Chen, T. T.; Xing, D. H.; Chen, X.; Li, J.; Wang, L. S. Observation of highly stable and symmetric lanthanide octa-boron inverse sandwich complexes. *Proc. Natl. Acad. Sci. U. S. A.* **2018**, *115*, E6972−E6977.
(39) Chen, T. T.; Li, W. L.; Li, J.; Wang, L. S. $[La(\eta^x\text{-}B_x)La]^-$($x$ = 7−9): a new class of inverse sandwich complexes. *Chem. Sci.* **2019**, *10*, 2534−2542.
(40) Li, W. L.; Chen, T. T.; Jiang, Z. Y.; Wang, L. S.; Li, J. Recent progresses in the investigation of rare-earth boron inverse sandwich clusters. *Chin. J. Struct. Chem.* **2020**, *39*, 1009−1018.
(41) Chen, X.; Zhao, Y. F.; Wang, L. S.; Li, J. Recent progresses of global minimum searches of nanoclusters with a constrained basin-hopping algorithm in the TGMin program. *Comput. Theor. Chem.* **2017**, *1107*, 57−65.
(42) Zhao, Y.; Chen, X.; Li, J. TGMin: A global-minimum structure search program based on a constrained basin-hopping algorithm. *Nano Res.* **2017**, *10*, 3407−3420.
(43) Chen, X.; Zhao, Y. F.; Zhang, Y. Y.; Li, J. TGMin: an efficient global minimum searching program for free and surface-supported clusters. *J. Comput. Chem.* **2019**, *40*, 1105−1112.
(44) Te Velde, G. T.; Bickelhaupt, F. M.; Baerends, E. J.; Fonseca Guerra, C.; van Gisbergen, S. J.; Snijders, J. G.; Ziegler, T. Chemistry with ADF. *J. Comput. Chem.* **2001**, *22*, 931−967.
(45) Guerra, C. F.; Snijders, J. G.; Te Velde, G. T.; Baerends, E. J. Towards an order-N DFT method. *Theor. Chem. Acc.* **1998**, *99*, 391−403.
(46) Baerends, E. J.; Ziegler, T.; Autschbach, J.; Bashford, D.; Bérces, A.; Bickelhaupt, F. M.; Yakovlev, A. L.; et al. *ADF 2017*; SCM, Inc.: Amsterdam, 2017.
(47) Perdew, J. P.; Burke, K.; Ernzerhof, M. Generalized gradient approximation made simple. *Phys. Rev. Lett.* **1996**, *77*, 3865−3868.
(48) Van Lenthe, E.; Baerends, E. J. Optimized Slater-type basis sets for the elements 1−118. *J. Comput. Chem.* **2003**, *24*, 1142−1156.
(49) Lenthe, E. v.; Baerends, E.-J.; Snijders, J. G. Relativistic regular two-component Hamiltonians. *J. Chem. Phys.* **1993**, *99*, 4597−4610.
(50) Adamo, C.; Barone, V. Toward reliable density functional methods without adjustable parameters: the PBE0 model. *J. Chem. Phys.* **1999**, *110*, 6158−6170.
(51) Dunning, T. H., Jr. Gaussian basis sets for use in correlated molecular calculations. I. The atoms boron through neon and hydrogen. *J. Chem. Phys.* **1989**, *90*, 1007−1023.
(52) Cao, X.; Dolg, M. Valence basis sets for relativistic energy-consistent small-core lanthanide pseudopotentials. *J. Chem. Phys.* **2001**, *115*, 7348−7355.
(53) Cao, X.; Dolg, M. Segmented contraction scheme for small-core lanthanide pseudopotential basis sets. *J. Mol. Struct.: THEOCHEM* **2002**, *581*, 139−147.
(54) Li, J.; Li, X.; Zhai, H. J.; Wang, L. S. Au_{20}: A tetrahedral cluster. *Science* **2003**, *299*, 864−867.
(55) Schipper, P. R. T.; Gritsenko, O. V.; van Gisbergen, S. J. A.; Baerends, E. J. Molecular calculations of excitation energies and (hyper) polarizabilities with a statistical average of orbital model exchange-correlation potentials. *J. Chem. Phys.* **2000**, *112*, 1344−1352.
(56) Zubarev, D. Y.; Boldyrev, A. I. Developing paradigms of chemical bonding: adaptive natural density partitioning. *Phys. Chem. Chem. Phys.* **2008**, *10*, 5207−5217.
(57) Mulliken, R. S. Electronic population analysis on LCAO-MO molecular wave functions. I. *J. Chem. Phys.* **1955**, *23*, 1833−1840.
(58) Hirshfeld, F. L. Bonded-atom fragments for describing molecular charge densities. *Theor. Chim. Acta* **1977**, *44*, 129−138.
(59) Wiberg, K. B.; Rablen, P. R. Comparison of atomic charges derived via different procedures. *J. Comput. Chem.* **1993**, *14*, 1504−1518.
(60) Bickelhaupt, F. M.; van Eikema Hommes, N. J. R.; Fonseca Guerra, C.; Baerends, E. J. The carbon-lithium electron pair bond in $(CH_3Li)_n$ (n = 1, 2, 4). *Organometallics* **1996**, *15*, 2923−2931.
(61) Swart, M.; van Duijnen, P. T.; Snijders, J. G. A charge analysis derived from an atomic multipole expansion. *J. Comput. Chem.* **2001**, *22*, 79−88.
(62) Zhai, H. J.; Kiran, B.; Li, J.; Wang, L. S. Hydrocarbon analogs of boron clusters: Planarity, aromaticity, and antiaromaticity. *Nat. Mater.* **2003**, *2*, 827−833.
(63) Sergeeva, A. P.; Popov, I. A.; Piazza, Z. A.; Li, W. L.; Romanescu, C.; Wang, L. S.; Boldyrev, A. I. Understanding boron through size-selected clusters: structure, chemical bonding, and fluxionality. *Acc. Chem. Res.* **2014**, *47*, 1349−1358.
(64) Boldyrev, A. I.; Wang, L. S. Beyond organic chemistry: Aromaticity in atomic clusters. *Phys. Chem. Chem. Phys.* **2016**, *18*, 11589−11605.

https://doi.org/10.1021/acs.jpca.1c01149
J. Phys. Chem. A 2021, 125, 2622−2630